Viscous flow behavior of tholeiitic and alkaline Fe-rich martian basalts

Magdalena Oryaëlle Chevrel, David Baratoux, Kai-Uwe Hess, Donald B Dingwell

Available online at www.sciencedirect.com

ScienceDirect

Geochimica et Cosmochimica Acta 124 (2014) 348–365

Geochimica et Cosmochimica Acta

www.elsevier.com/locate/gca

Viscous flow behavior of tholeiitic and alkaline Fe-rich martian basalts ☆

Magdalena Oryaëlle Chevrel [a,*], David Baratoux [b], Kai-Uwe Hess [a], Donald B. Dingwell [a]

[a] University of Munich (LMU), Department of Earth and Environmental Sciences, Theresienstr. 41/III, 80333 Munich, Germany
[b] University Toulouse III, Institut de Recherche en Astrophysique et Plantologie (IRAP), UMR 5277 CNRS UPS, 14, Avenue Edouard Belin, 31400 Toulouse, France

Received 8 February 2013; accepted in revised form 20 August 2013; available online 6 September 2013

Abstract

The chemical compositions of martian basalts are enriched in iron with respect to terrestrial basalts. Their rheology is poorly known and liquids of this chemical composition have not been experimentally investigated. Here, we determine the viscosity of five synthetic silicate liquids having compositions representative of the diversity of martian volcanic rocks including primary martian mantle melts and alkali basalts. The concentric cylinder method has been employed between 1500 °C and the respective liquidus temperatures of these liquids. The viscosity near the glass transition has been derived from calorimetric measurements of the glass transition. Although some glass heterogeneity limits the accuracy of the data near the glass transition, it was nevertheless possible to determine the parameters of the non-Arrhenian temperature-dependence of viscosity over a wide temperature range (1500 °C to the glass transition temperature). At superliquidus conditions, the martian basalt viscosities are as low as those of the Fe–Ti-rich lunar basalts, similar to the lowest viscosities recorded for terrestrial ferrobasalts, and 0.5 to 1 order of magnitude lower than terrestrial tholeiitic basalts. Comparison with empirical models reveals that Giordano et al. (2008) offers the best approximation, whereas the model proposed by Hui and Zhang (2007) is inappropriate for the compositions considered.

The slightly lower viscosities exhibited by the melts produced by low degree of mantle partial melting versus melts produced at high degree of mantle partial melting (likely corresponding to the early history of Mars), is not deemed sufficient to lead to viscosity variations large enough to produce an overall shift of martian lava flow morphologies over time. Rather, the details of the crystallization sequence (and in particular the ability of some of these magmas to form spinifex texture) is proposed to be a dominant effect on the viscosity during martian lava flow emplacement and may explain the lower range of viscosities (10^2–10^4 Pa s) inferred from lava flow morphology. Further, the differences between the rheological behaviors of tholeiitic vs. trachy-basalts are significant enough to affect their emplacement as intrusive bodies or as effusive lava flows. The upper range of viscosities (10^6–10^8 Pa s) suggested from lava flow morphology is found consistent with the occurrence of alkali basalt documented from in situ analyses and does not necessarily imply the occurrence of basaltic-andesite or andesitic rocks.

* Corresponding author.
E-mail addresses: oryaelle.chevrel@gmail.com, chevrel@min.uni-muenchen.de (M.O. Chevrel).

0016-7037/$ - see front matter © 2013 The Authors. Published by Elsevier Ltd. All rights reserved.
http://dx.doi.org/10.1016/j.gca.2013.08.026

1. INTRODUCTION

Both in situ and remote sensing-based chemical and mineralogical analyses of igneous rocks on Mars indicate the wide occurrence of Fe-rich tholeiitic basalts as well as Fe-rich mildly alkali- and trachy-basalts (13–22 wt.% of total iron content expressed as FeO_{tot}) (e.g., Binder, 1976; Gellert et al., 2004, 2006; McSween et al., 2004, 2006b; Boynton et al., 2007; Bost et al., 2012; Grott et al., 2013; Fig. 1). The chemical compositions of the martian basalts are significantly shifted toward Fe-rich compositions in comparison with terrestrial basalts (characterized by an average of FeO_{tot} abundance of ~12 wt.%). This specificity of the martian basalt reflects the mantle source which is enriched in iron in comparison with the terrestrial mantle as initially proposed from the martian meteorites analysis (Dreibus and Wänke, 1984, 1985). In detail, Dreibus and Wänke (1985) calculated the martian mantle composition by assuming a chondritic abundance of refractory lithophile elements in the mantle. Then, they used the nearly constant Fe/Mn ratio in martian meteorites, as the two elements are not significantly fractionated during magmatic processes. This calculation yields a martian mantle that contains twice as much Fe as the Earth's mantle with a Mg number (molar Mg/(Mg + Fe) ratio, noted Mg#) of 75 (terrestrial Mg# is 0.89). A Fe-rich composition is also inferred from evaluations of the internal structure of Mars using geophysical constraints including the moment of inertia (Anderson, 1972; Yoder, 2003; Khan and Connolly, 2008). It is also of note that the compositions of partial melts of an iron-rich mantle matches the mineralogy and chemistry of Mars' surface (Bertka and Holloway, 1994; El Maarry et al., 2009; Baratoux et al., 2011, 2013). The common occurrence of Fe-rich magmas inferred from in situ or remote-sensing

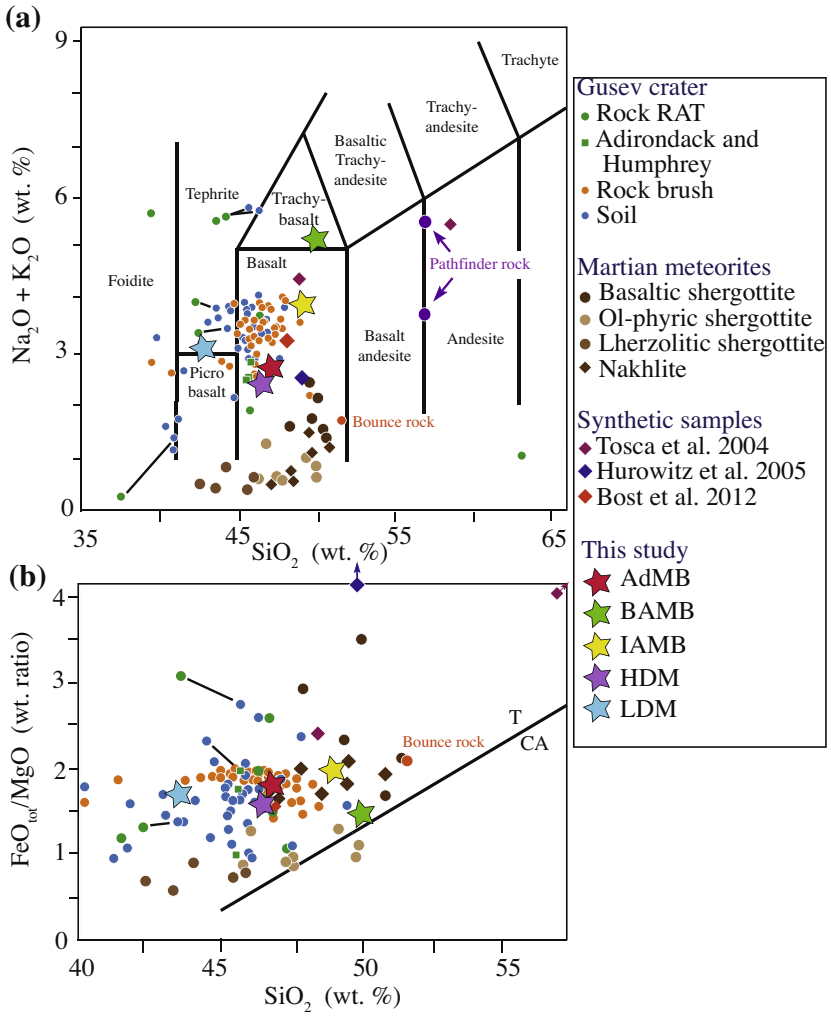

Fig. 1. Composition of the synthetic samples of this study (stars) plotted in the total alkalis ($Na_2O + K_2O$) and FeO_{tot}/MgO ratio vs. silica content (in wt.%) diagrams (modified figure from McSween et al., 2009 and Bost et al., 2012). The data includes the in situ analyzed rocks at Gusev craters (compositions of brushed rock and after abrasion, RAT, are connected by tie-lines), Pathfinder rocks and martian meteorites. The Bounce rock is the only sample of basaltic origin that was analyzed in the Meridiani Planum by the Opportunity rover (Rieder et al., 2004; Zipfel et al., 2004). Also shown for comparison are the synthetic Pathfinder rock and soil from Tosca et al. (2004), the synthetic Los Angeles sample from Hurowitz et al. (2005) as well as the synthetic sample from Bost et al. (2012).

observations is therefore unlikely to be a bias in our current knowledge of the Mars surface. Such Fe-rich magmas have been formed from the early history of Mars until the most recent volcanic activity.

In contrast to Mars, Fe-rich magmas on Earth are rare, being associated with the ultramafic archean lavas such as ferropicrite (Arndt et al., 1977); originating from a peculiar Fe-rich mantle source (Francis et al., 1999; Gibson et al., 2000) and/or hot spot related volcanism (Fisk et al., 1982; Stout et al., 1994; Norman and Garcia, 1999; Eason and Sinton, 2009); or resulting from melt immiscibility and phase separation at a late stage of the crystallization sequence as observed at the Skaergaard intrusion (e.g., Philpotts, 1977; Veksler, 2009). While the physical properties of Fe-rich melts have limited applications on Earth, they are of primary importance to understand the dynamics of volcanic materials on Mars. Recent martian lava flows (younger than 50 Ma) suggest the possibility of magma migrating through a 150–200 km thick lithosphere (Hartmann et al., 1999; Vaucher et al., 2009b; Hauber et al., 2011). Morphological characteristics of volcanic edifices with gentle slopes as well as long lava flows indicate effusive activity of very fluid lavas (e.g., Greeley et al., 2005; Hiesinger et al., 2007; Baratoux et al., 2009; Vaucher et al., 2009b) and layers of pyroclastic deposits hint at the existence of explosive activity (Hynek et al., 2003).

Viscosity is the main physical parameter affecting the evolution of molten bodies from their formation, during their ascent and emplacement in the subsurface as intrusions (Michaut, 2011; Taisne et al., 2011; Michaut et al., 2013) or at the surface as volcanic flows (e.g., Pinkerton and Stevenson, 1992; Dingwell, 1996). It controls the speed of magma ascent through the crust, the ease of crystal and bubble growth, and therefore defines the type of eruption. A lower viscosity implies a faster transport (or lower driving stresses) during both ascent and surface emplacement. Further, for the same initial concentration of volatiles, inefficiently degassed highly viscous bubbly magma experiences more explosive behavior whereas efficiently degassed low viscosity magmas erupt effusively. Knowing the viscosity of martian lavas is thus a key parameter for understanding the migration of magmas and morphology of volcanic landforms throughout the entire history of Mars.

The lava flow viscosity values inferred from morphological analysis on Mars range from 10^2 to 10^8 Pa s. These are attributed to ultrabasic, basaltic or more evolved compositions (Grott et al., 2013 and references therein). In fact, the occurrence of very fluid lavas on Mars represents a possible source of confusion for the recognition of channels associated with effusive flows against fluvial channels associated with liquid water flows. For instance, outflow channels have been principally associated to catastrophic water release (the dominant hypothesis) but an alternative possibility would be the effusion of low viscosity magmas (Leverington, 2011 and reference therein). The interpretation of landforms within one of the youngest regions of Mars, Central Elysium Planitia, has also been the focus of controversial interpretations (Jaeger et al., 2007, 2010; Page, 2008, 2010; Plescia, 1993; Vaucher et al., 2009a,b). Such ambiguities are a strong motivation for constraining the range of possible viscosities of martian lavas.

Low apparent viscosities are qualitatively compatible with the known compositions of martian basaltic rocks containing a relatively low Si and high Fe content (Greeley et al., 2005; Baratoux et al., 2009; Hauber et al., 2009; Vaucher et al., 2009a,b; Chevrel et al., 2012). However, the viscosity of such Fe-rich martian lavas has never been directly measured. The closest Fe-rich compositions that have been measured are some synthetic lunar lavas that have a lower viscosity than terrestrial basaltic lavas (Murase and McBirney, 1970; Cukierman et al., 1972). Here we measure the viscous behavior of Fe-rich martian lavas and test whether currently available empirical models relating the chemical composition to the melt viscosity (Shaw, 1972; Hui and Zhang, 2007; Giordano et al., 2008) are well adapted to the specificity and diversity of the martian lavas compositions.

The dry melt viscosity is investigated over a very wide temperature range: at superliquidus temperatures as well as at low temperatures (near the glass transition) in order to describe well their non-Arrhenian behavior (Hess and Dingwell, 1996; Russell and Giordano, 2005; Hui and Zhang, 2007; Giordano et al., 2008). The experimental viscosity results are then compared to terrestrial and lunar Fe-rich melts. The increase of viscosity caused by crystallization is then modeled and discussed as a function of the crystallization sequence at surface conditions. This study provides a framework to interpret the diversity of morphologies of effusive flows on Mars' surface, to address which empirical models may be used to calculate the viscosity of Fe-rich silicate melts that may be implemented in turn into models of intrusion emplacement or lava flow emplacement.

2. SAMPLES

The five samples investigated in this study are Fe-rich basalts chosen to be representative of the known diversity of martian basalts. Three samples have a chemical composition directly given by in situ Alpha Particle X-ray Spectrometer analysis (post rock-grinding) of volcanic rocks at Gusev crater on Mars. The selected compositions correspond to the chemical analyses of the Adirondack class rock, Irvine and Backstay rocks given in Ming et al., 2008 (Table 1). The Adirondack basalt is a dark, fine-grained, vesicular rock interpreted as lava. It is an olivine-rich primitive basalt with high Mg and low K (similar to a tholeiitic basalt). It is largely enriched in Fe and depleted in Al compared to common terrestrial tholeiitic basalt and is the dominant type on the Gusev plains (the Adirondack class rock referred here as AdMB). The Irvine and Backstay rocks (referred as IAMB and BAMB, respectively) are the first alkali basalts recognized on Mars and were found at the Columbia Hills inside the Gusev Crater. They are interpreted as lavas or possibly dike rocks. Backstay is enriched in Al and alkaline ($Na_2O + K_2O = 5$ wt.%) and depleted in Fe, Mn, and Cr compared to the Adirondack basalts. The Irvine class rocks are geochemically similar to Backstay except that they are depleted in Al, P, and alkaline elements

Table 1
Starting chemical composition (in wt.%) of the investigated martian synthetic melts. Composition of Adirondack class rock, Irvine and Backstay rocks are derived from Ming et al. (2008) after removing Cr, S and CO_2 and are normalized to 100 wt.%. Compositions of the melts formed by high and low degree of partial melting are calculated using MELTS for respectively 15% and 5% melting of the martian mantle composition given by Dreibus and Wänke (1984).

	Tholeiitic basalt Adirondack class rock	Mildly-alkaline basalt Irvine	Trachy-basalt Backstay	Melt formed by high degree of mantle partial melting	Melt formed by low degree of mantle partial melting
	AdMB	IAMB	BAMB	HDM	LDM
SiO_2	47.01	49.09	50.22	46.72	43.38
TiO_2	0.59	1.10	0.94	0.56	0.68
Al_2O_3	10.86	8.58	13.46	10.61	10.28
FeO_{tot}	19.43	20.36	13.87	18.99	21.19
MnO	0.42	0.38	0.24	0.11	0.14
MgO	10.14	9.82	8.43	11.39	11.73
CaO	8.09	5.99	6.12	8.41	8.20
Na_2O	2.66	3.10	4.21	2.25	3.03
K_2O	0.15	0.62	1.09	0.17	0.25
P_2O_5	0.65	0.97	1.41	0.79	1.13
Total	100	100	100	100	100

($Na_2O + K_2O = 3$ wt.%), and enriched in Fe with an average 19.7 wt.% FeO_{tot} compared to 13.2 wt.% FeO_{tot} in Backstay (McSween et al., 2006a; Ming et al., 2008).

The two other samples are compositions based on equilibrium melting calculations of a primitive mantle composition following Baratoux et al. (2011). According to this study, variations in the average surface composition of volcanic provinces may be related to variations of conditions of partial melting, providing evidence for cooling of the martian mantle over time. The inferred changes in conditions of partial melting (pressure, temperature) have been then shown to produce changes in mineralogy consistent with those inferred from spectroscopic observations, in particular for the pyroxene compositions (Baratoux et al., 2013). Therefore, two additional compositions corresponding to the end-members cases of these studies are considered. One composition is calculated for a pressure of 13 kbars and a potential temperature of the mantle of 1400 °C, corresponding to 15% of mantle partial melting (hereafter High Degree partial Melt: HDM); its composition is very similar to AdMB. A second composition is calculated at 17 kbars and for a potential temperature of the mantle of 1350 °C, corresponding to a low degree partial melt (LDM) of ~5%. LDM is poorer in Si and richer in Fe relatively to all other studied compositions (Table 1). These compositions neglect possible variations of the source and extraction from distinct geochemical reservoirs that have been previously depleted (e.g., during the magma ocean scenario – Elkins-Tanton et al., 2005, or related to volcanism). Nevertheless, these compositions offer a framework to study the rheological consequences of the variations of conditions of partial melting.

3. EXPERIMENTAL METHODS

3.1. Melt preparation

The starting chemical compositions used for the synthesis are Cl-, S- and Cr-free to prevent volatility and early crystallization of Cr-rich oxides (Table 1). The samples were prepared by mixing 100 g of dried (120 °C) reagent grade oxide and carbonate powders of SiO_2, Al_2O_3, MgO, $CaCO_3$, Fe_2O_3, TiO_2, MnO, Na_2CO_3, K_2CO_3 and NaH_2PO_4 based on the compositions given in Table 1. The powder mixes were milled together in an large agate mortar in acetone for at least 30 min and then fused in a platinum crucible for two hours in air at 1500 °C. The melts were then poured on a copper plate, crushed and melted a second time. Those melts were then poured directly into a thick-walled cylindrical platinum crucible that was transferred to a furnace equipped with a rotational viscometer and stirred for five hours using a $Pt_{80}Rh_{20}$ spindle at 1500 °C. The crucibles and spindle had been previously doped with Fe to minimize the propensity of Fe loss into the crucible wall.

3.2. Superliquidus viscometry under controlled oxygen fugacity

The viscosity at superliquidus conditions was measured via the concentric cylinder method (Shaw, 1969; Dingwell, 1986) at 1 atm and under varying ambient oxygen fugacity (in air and down to two orders of magnitudes below the Quartz–Fayalite–Magnetite buffer, noted QFM-2). The setting consists of a cylindrical crucible containing the molten material that is placed in the hot zone of a vertical furnace equipped with a gas-tight alumina muffle tube and a CO_2–CO gas-mixing line (Dingwell and Virgo, 1987). A cylindrical spindle is inserted into the melt and is driven at constant speed by a viscometer head (Brookfield DVIII+) that records the torque. The torque is converted into viscosity using a standard glass (DGG-1) calibration. The precision on the viscosity for this apparatus was determined by Dingwell (1986) from the sum of the precision of standard and sample determination and is ±5%. The temperature calibration was determined by the immersion of a B-type (Pt/Pt_{90}–Rh_{10}) thermocouple into the melt over a large range of temperatures and does not exceed ±1 °C.

For each composition, the viscosity was first measured in air from 1500 °C to 1375 °C by 25 °C increments of decreasing temperature. The effect of the melt redox-state on viscosity was then investigated at isothermal condition (1385 or 1395 °C) by decreasing the oxygen fugacity inside the muffle tube via changing the $CO:CO_2$ ratio of the gas flow. At the lowest ambient oxygen fugacity, usually corresponding to QFM-2, the temperature dependence of viscosity was also measured between 1500 °C and 1375 °C. The viscosity, temperature and oxygen fugacity were recorded all along the experiments at every second, which allows precise tracking of the melt response. The viscosity values were taken after 1 h of isothermal equilibrium for measurements performed at constant fO_2 and after a minimum of 24 h for each fO_2 change to ensure a melt fully equilibrated with the new fO_2. At the end of the experiment, the viscosity was measured again at the highest temperature in air to check a possible instrumental drift.

The melts were sampled at high temperature and at every fO_2 step (each sampling batch is labeled between -S0 to -S8). The quenching method, called the "dip-quench" method, consists in inserting and removing an alumina rod (with a diameter of 3 mm) into the liquid forming a melt droplet on the rod tip that is then fast quenched into a water bucket. The process lasts less than 15 s and the melt cooling rate is then estimated to be ~100 °C/s. This fast cooling is necessary to avoid crystallization and causes the glass to fragment into powder and tens of small chips (<10 mg) that were used for further analyses (chemical analyses, redox state titration, calorimetric measurements).

3.3. Chemical composition and redox state

One or two chips per sampling batch resulting from the "dip quench" were mounted as polished sections for petrographic and chemical analysis carried out with a CAMECA SX 100 Electron MicroProbe Analyser (EMPA), and Back Scattered Electron images (BSE) were obtained for each analyzed chip. About 30 mg of powder was used for redox state determination performed using potassium dichromate titration. This procedure is a destructive technique that digests the material and measures the amount of Fe^{2+} by a redox reaction (Giuli et al., 2011). In combination with EMPA analysis, the FeO/FeO_{tot} ratio was calculated for each glass.

3.4. Low temperature viscosity at the glass transition temperature

The viscosity at sub-liquidus conditions was determined from quenched glassy chips briefly heated into the metastable supercooled liquid state. The excursions into the metastable state required by the parallel plate or beam-bending techniques cannot be used because of rapid crystallization of Fe-rich samples (Karamanov and Pelino, 2001; Karamanov et al., 2002; Bouhifd et al., 2004). An alternative method is to evaluate the viscous relaxation time that can be fixed to the glass transition at a known quenching/heating rate.

The temperature of the glass transition is defined as the limiting fictive temperature (T'_f) that is the temperature at which the structure of the liquid is frozen in during quenching; T'_f is therefore a function of the quench rate of the liquid: the faster the quench rate, the higher T'_f. The glass transition temperature range can be determined with calorimetric measurements because the sample releases some excess in heat capacity when it is heated from the glass field into the liquid field (endothermal peak of the heat capacity vs. temperature/time curve; e.g., Moynihan et al., 1974; Scherer, 1984).

About 27 mg of glass (usually 4–5 chips) per sample batch were used for calorimetry measurements using the differential scanning calorimetry (DSC; 404 Pegasus apparatus from NETZSCH Gerätebau). All samples received the same treatment; they were initially heated at 20 °C/min, and then cooled and subsequently re-heated at identical rates of 25, 20, 15 and 10 °C/min in a raw. The curves were calibrated against a baseline and the heat capacity (Cp) was calculated with a sapphire standard of 27.7 mg. The Cp values are used here as relative changes and not in terms of the absolute Cp values. For all samples, T'_f was obtained from the re-heating sample curves having known quenching rates using the method described by Moynihan (1995). The corresponding viscosity is then calculated via the linear relationship between the applied cooling rate and the viscosity (Gottsmann et al., 2002) at T'_f:

$$\log \eta = K - \log |q| \quad (1)$$

where η is the viscosity (Pa s), K is a constant that equals to 11.04 ± 0.37 as determined at T'_f by Chevrel et al. (2012) and q is the cooling rate in K s^{-1}.

4. RESULTS: COMPOSITIONS AND REDOX STATE

4.1. Chemical compositions

The chemical composition of each sampling batch was analyzed in order to check the stability of the element concentration during the viscosity measurements. Minimums of 20 chemical analyses data across a single chip were performed to evaluate the chemical homogeneity of the glasses (Table A.1 in Supplementary material).

For the samples equilibrated in air, the results indicate that the samples are chemically homogeneous within the error of the measurements. These compositions are slightly enriched in Fe and depleted in Si compared to the starting composition (dark red symbols in Fig. 2). Only one sample, IAMB-S1, was recognized to contain some micro-oxide crystals with a length of <10 μm are unequally distributed. The entire BSE picture of the sample chip was observed and the area covered by the crystals was estimated (using ImageJ software) to represent less than 0.5%. Their effect is therefore neglected for viscosity measurements (Lejeune and Richet, 1995). An attempt to measure their composition is given in Table A.2. Tinier crystals are found around these oxides and have a dendritic morphology, typical of rapid growth during quenching process.

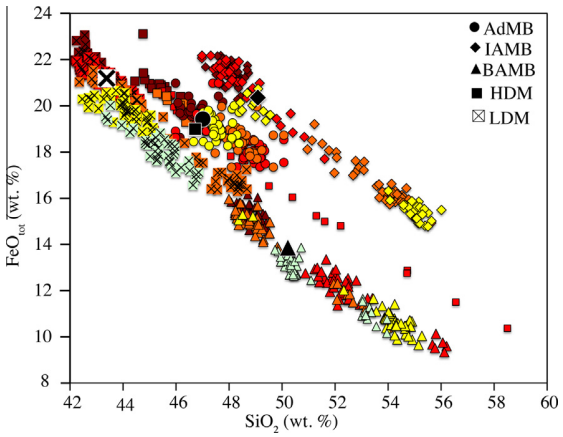

Fig. 2. Microprobe chemical composition analyses of each investigated samples. The symbol shape differs for each composition as indicated in the legend. The black symbols are the starting chemical composition (according to the weighted regent powders). The color code indicates the change is fO_2 conditions: the more oxidized (equilibrated in air) is in dark red, then in order toward more reduced: red, orange, yellow, and whitish.

For the samples equilibrated under reduced conditions, no oxide crystal was found but the chemical compositions of the glasses are more variable (Table A.1, Fig. 2). For AdMB, although each individual sample is homogeneous, the samples having different redox states have different compositions. AdMB-S3, -S4 and -S8 are enriched in SiO_2 (48.3–49.1 wt.%) and depleted in FeO_{tot} (16.9–18.6 wt.%) compared to the others that have a composition close to the starting material and within the standard deviation of the analyses ($SiO_2 = 46$–47.6 wt.% and FeO = 18.6–20.9 wt.%). There is no clear trend correlating the variation of chemical composition and quenching conditions. The BAMB and IAMB samples show large variations between all the samples, and a single chip may exhibit a distinct internal heterogeneity. For most of these samples, two distinguishable compositions could be

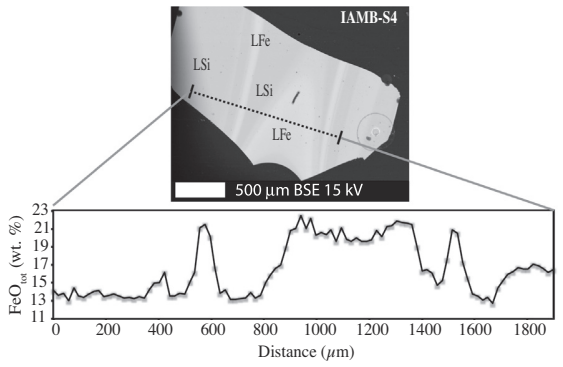

Fig. 3. Back Scattered Electron image and chemical profile of IAMB-S4 glass chip obtained by 'dip quench' from 1395 °C and low fO_2. The grey intensity is scaled on the presence of heavy elements, the brighter the higher FeO_{tot} and the lower SiO_2 evidencing two different compositions (LFe and LSi).

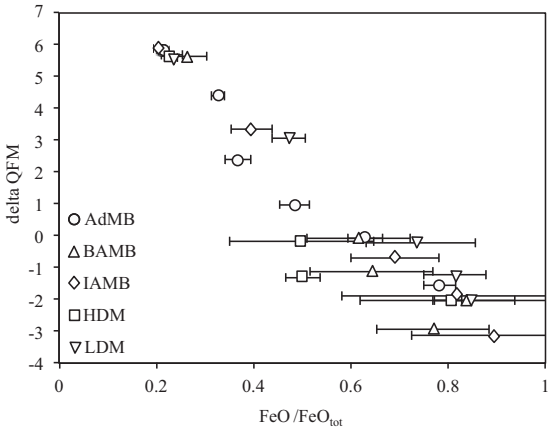

Fig. 4. Redox state (FeO/FeO_{tot}) of the melts as a function of the ambient fO_2 express as delta QFM.

identified; given as LSi for liquid enriched in Si and LFe for liquid enriched in Fe (Table A.1). Although for most of the samples, this compositional variation was not observed with BSE images, some filaments of distinct compositions were observed within IAMB-S4 (Fig. 3). The HDM and LDM samples quenched under different conditions have also variable chemical compositions. In sample HDM-S2, two distinct compositions, LSi, and LFe, could be identified. The sample LDM-S3 has the larger internal heterogeneity, with SiO_2 varying from 42.3 to up to 49.4 wt.% and FeO_{tot} from 21.5 down to 15.9 wt.%. For most of the samples, although chemical heterogeneity could be detected, the use of BSE images does not permit the identification of sub-micron emulsion or a gradient of elemental diffusion. These heterogeneities are discussed in the Section 4.3.

4.2. Iron redox-state

Two titrations were performed for each sample batch and the difference were less than 0.8 wt.% of FeO. The FeO/FeO_{tot} was calculated with the average FeO values of the two titrations and the average FeO_{tot} from EMPA measurement for each sample (Fig. 4). Taking into account the variation of the titration and of EMPA measurements, the error on the redox state is calculated for each sample. The largest error is calculated for the reduced samples, where the compositional variation is greatest. The observed chemical heterogeneity within a single sample raises significant concerns over the quality of the redox-state calculations. These results suggest that the sampling technique must be improved further to reduce the error bars on the redox-state.

4.3. Evidence of immiscibility at high-temperature or phase separation during slow quenching?

Whether the chemical heterogeneity observed in the quenched samples is due to liquid immiscibility at high-temperature or to the quenching process is a major issue

(Veksler et al., 2007, 2008; Philpotts, 2008). Unlike in static experiments (melt droplet suspended to Pt-loop wire), liquid separation may happen in dynamic experiments (Veksler et al., 2007, 2008). The stirring of the melt during viscosity measurement by the spindle is fast, achieving a speed of 40 rotations per minute and may then enhance phase separation. As obtained in previous studies, we observe here that the composition of the mafic conjugate liquid (LFe) is close to the bulk starting material, and the felsic member of the pair (LSi) is enriched in Si, as expected in the case of immiscibility processes. However, although we did not conduct any experiment that could prove the occurrence of two liquids at high temperature, we note that immiscibility has never been reported at such high temperatures apart from pure FeO–SiO_2 binary systems (Roedder, 1978; Philpotts, 2008). Moreover, during the viscosity measurement, the presence of two immiscible liquids would cause a strain-rate dependent viscosity (as in the case of suspended deformable bubbles) that was not observed. It seems therefore unlikely that immiscible liquids were present during the viscosity measurement.

A phase separation during quenching is more likely to have happened. An attempt to quench these melts was first made by pouring the melt (equilibrated in air at 1500 °C) onto a copper plate and pressing it together with another copper plate. The resulting piece of glass was 3 mm thick and had near parallel surfaces. Chemical analyses were carried out along a vertical profile within the sample; this revealed a variation in chemical composition extending from outer quenched surfaces to the glass interior. The inner core was enriched in Fe while the surfaces were Si-rich. No other significant elemental variations were noted. Such variations were also observed in Wilson et al. (2012), and were attributed to a quenching rate, which was too slow to permit formation of a homogeneous glass. This chemical profile is a clear indicator of elemental migration, and eventually melts separation during quenching. In order to achieve a faster quench rate, avoiding such chemical variation, and also to be able to quench reduced samples, the "dip quench" technique was favored and always applied. However, even by using this technique, the produced glasses tend to be heterogeneous (internally or across the sample series). For the oxidized sample, dendritic crystals could grow during quenching but for the reduced samples, phase separation seems favored. Moreover, it was not possible to maintain a reduced environment during the quenching process; the reduced melts are quenched in oxidized environment (air). Even if this process is fast, estimated at 100 °C/s (from 1400 to 20 °C in ~15 s), the small withdrawn droplet may have sufficient time to become oxidized, favoring the migration and redistribution of the elements. An indicator that elements can migrate during the quenching was observed by the chemical analyses carried out on small chips that were preserved sticking to the sampling alumina rod, along a profile from the rod outward (Fig. 5). On these transects the amount of Fe decreases and Si increases toward the spindle, accompanied by Al content slightly increasing by 1 wt.% (within the first 600 μm).

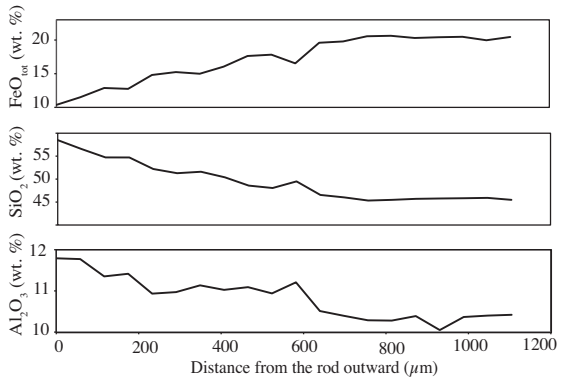

Fig. 5. Chemical profile taken from the rod outward across the HDM-S2 glass obtained by 'dip quench'.

In conclusion, it seems likely that the chemical variations observed in the glasses are due to phase separation during quenching. It is well known that the basaltic compositions may be bad glass formers, and this impedes efforts to produce homogeneous amorphous materials. The high Fe content of the melts in this study enhances this behavior. It is obvious that the "dip quench" procedure is questionable as a method for synthesis of homogeneous Fe-rich glasses; in particular for reduced melts. More experiments should be carried out to confirm the melt immiscibility. Static experiment using martian basaltic compositions should be first undertaken and then dynamic experiments using a centrifuge at high temperature and under reduced condition should be carried out. The sampling technique used here may be improved by permitting faster quenching and/or under sustained reducing conditions (Cukierman et al., 1973). Transmission electron microscopy technique may also be required to collect further evidence of any such micro or sub-micron scale features.

5. RESULTS: MELT VISCOSITY AND COMPARISON WITH MODELS

5.1. Viscosity in the superliquidus regime

The temperature dependence of viscosity measured in air and under low oxygen fugacity (near QFM-2) is presented in Table 2. In the investigated high temperature range, the melts have viscosities between −0.6 to 0.4 log Pa s; the trachy-basalt, BAMB, is an exception to this, with a viscosity 0.5 log Pa s higher than the others, attributed to higher Si and lower Fe content. Within the high temperature viscosity range, the temperature dependence of viscosity can be approximated by an Arrhenian relationship Shaw (1972):

$$\ln \eta = A_{\mathrm{Arr}} + E^*/RT \quad (2)$$

where A_{Arr} and E^* (kJ/mol) are the pre-exponential term and the activation energy of viscous flow, respectively and R the gas constant. For all compositions, the activation energy is calculated to be between 121 and 209 kJ/mol (Table 3). Investigation of temperature dependence of

Table 2
The viscosity of all investigated melts at 1 atm in air and at under reduced oxygen fugacity. The errors on the viscosity measurements at superliquidus conditions are estimated to be ±5%, except for the LDM melt measurements that showed a noisy torque reading. The errors on the viscosity near the glass transition are estimated to be ±0.37 log Pa s.

	Air			Reduced		
	T (°C)	log η (Pa s)	Error	T (°C)	log η (Pa s)	Error
AdMB	1483	−0.10	0.005	1385	0.17	0.010
	1458	−0.03	0.002	629	11.42	0.37
	1434	0.04	0.002	628	11.52	0.37
	1409	0.12	0.006	625	11.64	0.37
	1385	0.21	0.010	620	11.82	0.37
	1360	0.30	0.015			
	1336	0.39	0.020			
	647	11.42	0.370			
BAMB	1482	0.36	0.018	1395	0.56	0.028
	1457	0.44	0.022	1370	0.65	0.033
	1432	0.53	0.026	1346	0.75	0.037
	1407	0.62	0.031	1321	0.85	0.042
	1383	0.71	0.036	1296	0.95	0.048
	1358	0.82	0.041	1271	1.06	0.053
	1333	0.92	0.046	1247	1.18	0.059
	1308	1.03	0.052	1222	1.30	0.065
	1284	1.14	0.06	654	11.42	0.37
	674	11.42	0.370	657	11.52	0.37
				656	11.64	0.37
				653	11.82	0.37
IAMB	1483	−0.07	0.003	1395	0.14	0.007
	1458	0.00	0.000	1358	0.22	0.011
	1434	0.08	0.004	1334	0.30	0.015
	1409	0.16	0.008	632	11.42	0.37
	1385	0.24	0.012	625	11.52	0.37
	1360	0.33	0.016	623	11.64	0.37
	1336	0.42	0.027	619	11.82	0.37
	632	11.51	0.370			
HDM	1494	−0.31	0.015	1494	−0.34	0.017
	1469	−0.25	0.012	1469	−0.28	0.014
	1445	−0.19	0.009	1445	−0.22	0.011
	1420	−0.11	0.006	1420	−0.17	0.008
	1395	−0.04	0.002	1395	−0.11	0.005
	650	11.51	0.370	1370	−0.02	0.001
				638	11.42	0.37
				636	11.52	0.37
				631	11.64	0.37
				624	11.82	0.37
LDM	1492.96	−0.38	0.119	1395	−0.20	0.060
	1468.32	−0.32	0.082	1519	−0.41	0.150
	1443.69	−0.25	0.042	1494	−0.45	0.082
	1419.05	−0.17	0.083	1469	−0.32	0.106
	1394.42	−0.10	0.073	1445	−0.27	0.073
	1369.78	−0.02	0.066	1420	−0.23	0.072
	1492.96	−0.38	0.084	1395	−0.12	0.066
	624.85	11.51	0.370	1494	−0.32	0.086
				1445	−0.33	0.056
				1395	−0.16	0.048
				631	11.42	0.37
				626	11.52	0.37
				624	11.64	0.37
				620	11.82	0.37

viscosity at reduced condition reveals that the activation energy is similar for oxidized and reduced melts (± 10–20 kJ/mol).

The effect of redox-state on viscosity was investigated at a fixed temperature under successive reducing oxygen fugacity until a minimum value is reached at approximately

Table 3
Arrhenian fitting parameters (A and E^*) for the viscosity data within the single superliquidus regime (at high temperature, HT) and near the glass transition (low temperature ranges, LT).

	A_{Arr} HT	E^* HT (kJ/mol)	A_{Arr} LT	E^* LT (kJ/mol)
AdMB-S2	−12.68	182	–	–
AdMB-S6	–	–	−62.40	666
BAMB-S0	−13.55	209	–	–
BAMB-S1	−13.42	204	−82.11	820
IAMB-S1	−12.45	179	–	–
IAMB-S4	−11.62	164	−35.27	462
HDM-S1	−11.01	151	–	–
HDM-S4	−10.30	140	−32.53	446
LDM-S1	−11.93	162	–	–
LDM-S5	−9.11	121	−48.38	561

Table 4
The viscosity at superliquidus regime of the investigated melts at various ambient fO_2. The fO_2 was measured by B-type sensors around the melt and it is different than the fO_2 inside the melt. The redox state of the melt is given by the FeO/FeO_{tot} ratio that is measured from oxido-reduction reaction (Fe-titration) done on the glass samples.

Sample	Temperature (°C)	log (fO_2)	log QFM	FeO/FeO_{tot}	log η (Pa s)	Duration (h)
AdMB-S2	1385	−0.63	5.84	0.21	0.21	39
AdMB-S3	1385	−2.08	4.40	0.33	0.15	120
AdMB-S4	1385	−4.08	2.39	0.37	0.14	70
AdMB-S5	1385	−5.48	0.99	0.48	0.12	96
AdMB-S6	1385	−6.55	−0.07	0.63	0.09	48
AdMB-S8	1385	−8.02	−1.55	0.78	0.17	96
BAMB-S0	1495	−0.74	5.65	0.26	0.67	–
BAMB-S1	1395	−6.48	−0.09	0.62	0.56	92
BAMB-S2	1395	−7.49	−1.11	0.64	0.56	38
BAMB-S3	1395	−8.41	−2.03	0.84	0.55	66
BAMB-S4	1395	−9.34	−2.96	0.77	0.58	51
IAMB-S1	1395	−0.61	5.89	0.21	0.32	24
IAMB-S2	1395	−3.16	3.33	0.40	0.22	46
IAMB-S3	1395	−7.18	−0.69	0.69	0.16	48
IAMB-S4	1395	−8.39	−1.89	0.82	0.14	46
IAMB-S5	1395	−9.63	−3.13	0.88	0.17	40
HDM-S1	1395	−0.70	5.68	0.23	−0.04	38
HDM-S2	1395	−6.58	−0.19	0.50	−0.09	41
HDM-S3	1395	−7.69	−1.30	0.50	−0.13	47
HDM-S4	1395	−8.41	−2.03	0.80	−0.09	39
LDM-S1	1395	−0.78	5.61	0.23	−0.23	24
LDM-S2	1395	−3.34	3.05	0.47	−0.16	44
LDM-S3	1395	−6.60	−0.21	0.74	−0.21	44
LDM-S4	1395	−7.63	−1.24	0.81	−0.16	45
LDM-S5	1395	−8.41	−2.03	0.85	−0.20	42

$FeO/FeO_{tot} = 0.6$ (Table 4 and Fig. 6). The maximum drop in viscosity is 0.18 log Pa s for IAMB. Further reduction ($FeO/FeO_{tot} > 0.6$) induces a slight but systematic increase in viscosity of less than 0.05 log Pa s that may be attributed to the change in Fe coordination state in the melt structure (Mysen, 1991). In such reduced conditions, to avoid the loss of Fe into the crucible wall (forming an alloy with the platinum) or the formation of metallic Fe nano-droplets, the experiments were always stopped when the torque started increasing.

The comparison of our measurements with the empirical models of Shaw (1972), Giordano et al. (2008, here after GRD) and Hui and Zhang (2007) is presented in Fig. 7 to assess which of these models are most appropriate to estimate the viscosity–temperature relationship of martian compositions. The Arrhenian model of Shaw that is based on basaltic compositions, yields results differing from experimental data with a root mean square error (RMSE) of 0.18 log unit for oxidized and 0.15 log unit for reduced melts. The GRD model, based on non-Arrhenian behavior and including a wider range of composition (from basaltic to rhyolite melts) differs from experimental data with a RMSE of 0.16 log unit for oxidized and 0.15 log unit for reduced melts, respectively at superliquidus condition. The model of Hui and Zhang significantly deviates from the experimental data set with a RMSE of 0.85 log unit

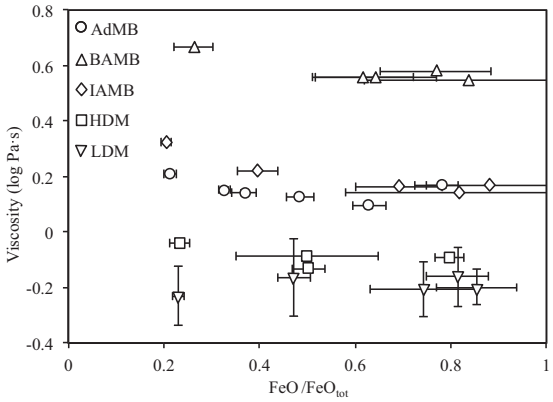

Fig. 6. The viscosity at superliquidus regime of the investigated melts as a function of their redox state expressed as FeO/FeO_{tot}.

for oxidized and 0.99 log unit for reduced melts. The Shaw and GRD models are therefore reproducing best the experimental data at high-temperature viscosity.

5.2. Calorimetric glass transition

The limiting fictive temperatures at the glass transition are given in Table 5 for all the samples. The quality and the reproducibility of the calorimetric curves ensure our ability to determine the glass transition temperature and depend strongly on the stability of the glass. The heat capacity curves of the oxidized samples show a typical endothermic peak at the glass transition through heating. However as observed in Chevrel et al. (2012), the stable liquid field cannot be reached because of the onset of crystallization immediately above the glass transition (exothermal peak; Fig. 8a). Even with a high cooling and subsequent heating rate of 25 °C/min or when the heating is stopped just after the peak, subsequent glass transition measurements on the same sample are shifted to higher temperatures. This shift toward high temperature may be attributed to the change of melt composition because of some crystallization or change in redox-state. For the most oxidized sample, a good reproducibility of the measurements was therefore not possible and the relationship between the glass transition temperature and the cooling history was biased (inverse relationship between cooling rate and T'_f).

In contrast, the reduced samples measurements were reproducible (within 3 °C), and the relation between T'_f and the cooling rate is consistent with previous studies (Fig. 8b). However, the shape of the heat capacity curve shows peculiar patterns. The heat capacity curves of the BAMB set of samples show very broad peaks forming a plateau of ~30 °C (Fig. 8c). It was also noted that for

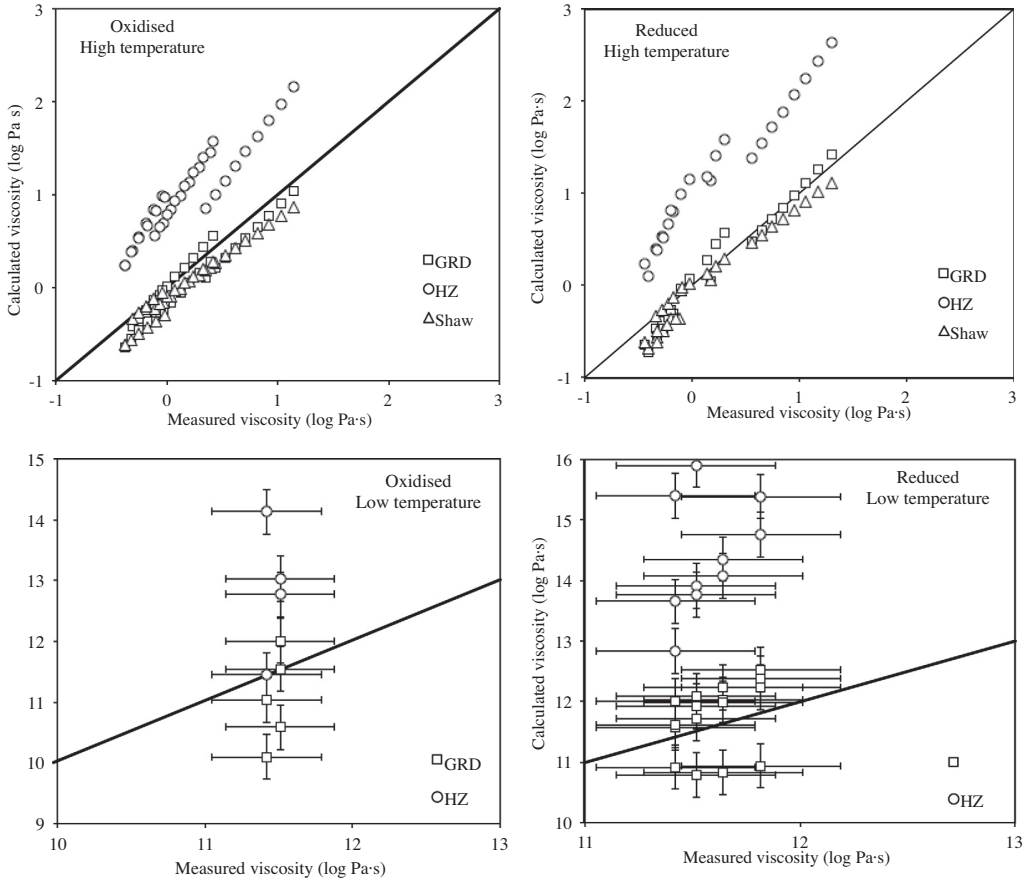

Fig. 7. Comparison of the measured viscosity in air and under reduced oxygen fugacity (at 1 atm) with the calculated viscosity via empirical models: Shaw (1972); GRD, Giordano et al. (2008); HZ, Hui and Zhang (2007).

Table 5
Limiting fictive temperatures (T'_f) estimated from the heat capacities curves measured after various cooling and subsequent heating rate of 25, 20, 15 and 10 °C/min.

Cooling rate (°C/min)	T'_f (°C)			
	25	20	15	10
AdMB-S2	670	–	–	–
AdMB-S4	635	659	666	664
AdMB-S5	630	636	636	638
AdMB-S6	629	628	625	620
AdMB-S8	637	635	631	628
BAMB1-S0	673	–	–	–
BAMB1-S1	654	657	656	653
BAMB1-S2	635	635	634	629
BAMB1-S3	646	643	640	628
BAMB1-S4	654	652	647	641
BAMB1-S5	647	646	643	638
IAMB-S1	–	632	–	–
IAMB-S2	–	–	–	–
IAMB-S3	634	630	627	627
IAMB-S4	632	625	623	619
IAMB-S5	628	625	618	615
HDM-S1	–	650	–	–
HDM-S2	638	637	632	629
HDM-S3	646	642	639	632
HDM-S4	638	636	631	624
LDM-S1	–	–	–	–
LDM-S2	–	–	–	–
LDM-S3	624	622	618	612
LDM-S4	623	620	617	611
LDM-S5	631	626	624	620

IAMB samples, a second peak was reached after some 100 °C after the first peak (Fig. 8d). In the literature there are unfortunately no studies about double or broad peaks. Only Kremers et al. (2012) observed a double peak that they interpreted to be the mingling of two glasses with the same composition but different redox state within a single sample. Here, no direct proof of variable redox state could be obtained, however in our study the chemical heterogeneity (previously discussed) may be the reason for such features. The difference in glass transition temperature calculated with the GRD model at $\eta = 10^{12}$ Pa s between the two conjugate melts (LFe and LSi) in the BAMB-S1 samples is of 20 °C and seems to correlate with the broad peak dimension. However, for IAMB-S4-LFe and -LSi melts, the glass transition temperature difference calculated with the GRD model at $\eta = 10^{12}$ Pa s, is of about 11 °C; therefore the two peaks in Fig. 8d are too far apart to be attributed to only variable compositions and redox changes might be additionally involved. Although it may not be the case as a general rule, the melt with less Si and more Fe (LFe) is expected to have a lower glass transition temperature than the conjugate Si-rich, Fe-poor melt (LSi). Hence, the first peak may correspond to the Fe-rich melt, the closer to the initial composition and the second peak to the Si-rich melt.

In order to get the best estimate of the glass transition temperature for the samples, we therefore preferred to estimate the limiting glass transition temperature (T'_f) only for the first peak, and at the onset of broad peak, that are the most likely to correspond to the composition which is both the most Fe-rich and closer to the starting melt composition.

5.3. Viscosity near the glass transition

Despite the challenges discussed above, total temperature errors (instrumental errors plus standard deviation from repeated measurements) are within ±4 °C. The temperature dependence of viscosity near the glass transition is calculated and the error on the viscosity values is estimated at ±0.37 log Pa s. As mentioned above, the relationship between T'_f and the cooling rate was difficult to obtain for the oxidized samples. The best estimation was therefore obtained with the first heating segment after controlled cooling rate (20 or 25 °C/min). The viscosity calculated at T'_f with the GRD and Hui and Zhang models are compared with the values estimated here (Fig. 7). The GRD model produces viscosity values within the errors associated with the calorimetric method with RMSE of 0.86 log unit for oxidized and 0.63 log unit for reduced samples, while the Hui and Zhang model yields results exceeding the measured values by several of orders of magnitude with a RMSE of 4.9 log unit for oxidized and 5.85 log unit for reduced samples. Only the GRD model is therefore adequate to estimate the viscosity–temperature relationship near the glass transition temperatures, though improvements should be done to incorporate such Fe-rich composition and redox-state in the model.

The parameters of the Arrhenian relationship (Eq. 1) near the glass transition temperature could not be obtained for the oxidized sample as only one viscosity data point was obtained. The fitting parameters for the reduced samples are given in Table 3.

5.4. Non-Arrhenian parameterization over the entire range of temperature

The entire viscosity data set for the oxidized and the reduced melts is fitted with a non-Arrhenian empirical relationship given as the Tammann–Vogel–Fulcher equation:

$$\log \eta = A_{TVF} + B_{TVF}/(T - C_{TVF}), \quad (3)$$

where T is melt temperature (K) and A_{TVF} represents a lower limit of silicate melt viscosity at infinite high temperature, and is approximately the same for all silicate melts (Mysen, 1955; Eyring et al., 1982; Angell, 1985; Russell et al., 2002, 2003). The optimal value for A_{TVF} is still debated but, here, the data were fitted using a preferred value for Fe-rich basaltic melts of -4.125 ± 0.4 (Chevrel et al., 2012) that slightly improves the quality of the fit compared to the common value proposed by the GRD model ($= -4.55 \pm 0.21$). The B_{TVF} and C_{TVF} parameters depend on the melt chemical composition. All parameters are given in Table 6.

In Fig. 9, the results are compared with the viscosity of some selected terrestrial and lunar Fe-rich basalts. At superliquidus conditions, the martian basalts viscosities

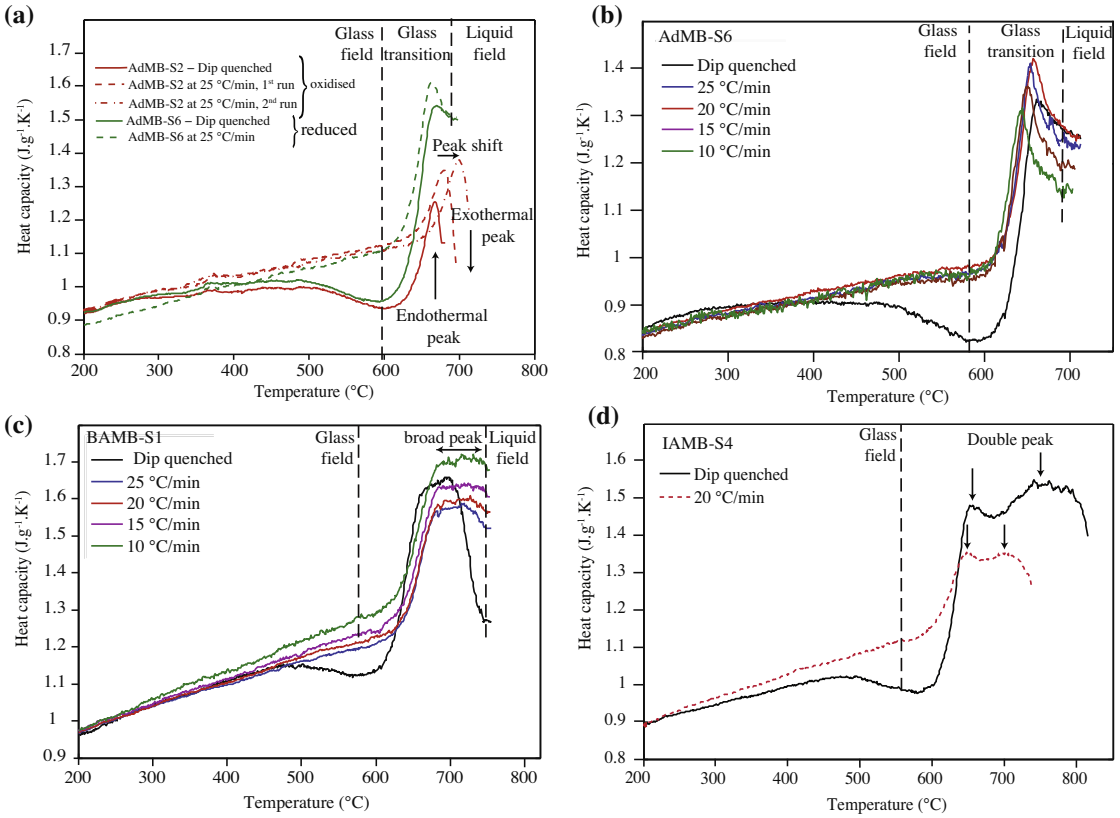

Fig. 8. Heat capacity curves as a function of temperature. (a) Example of sample AdMB-S2 equilibrated in air and AdMB-S6 equilibrated under reduced condition. The sample equilibrated in air shows crystallization (exothermal peak) after the glass transition is crossed and repeated measurements of the glass transition temperature are shifted to higher temperature. In contrast the sample equilibrated under low oxygen fugacity are reproducible and no crystallization occurs. (b) Example of sample AdMB-S6 that shows a normal evolution of the glass transition temperature vs. cooling rate. (c) Example of sample BAMB-S1 that shows broad peak at the glass transition. (d) Example of sample IAMB-S4 that shows the occurrence of double peaks.

Table 6
Fitting parameters of the TVF equation for the oxidized and reduced melts using a common A_{TVF} value T_f' is the limiting fictive temperature obtain for a cooling and subsequent heating rate of 10 °C/min.

	A_{TVF} (log Pa s)	B_{TVF} (log Pa s/K)	C_{TVF} (K)	RMSE[a]	T_f' 10/10
AdMB-S2	−4.125	4456	633.3	0.038	–
AdMB-S6	−4.125	4420	617.3	0.045	620
BAMB-S0	−4.125	4975	626.9	0.053	–
BAMB-S1	−4.125	4819	621.5	0.101	653
IAMB-S1	−4.125	4583	611.9	0.036	–
IAMB-S4	−4.125	4419	616.6	0.116	619
HDM-S1	−4.125	4185	655.3	0.038	–
HDM-S4	−4.125	4208	637.4	0.131	624
LDM-S1	−4.125	4216	628.0	0.034	–
LDM-S5	−4.125	4175	632.6	0.085	620

[a] Root Mean Square Error.

are as low as those of the Fe–Ti-rich lunar basalts and among the lowest viscosity recorded for the terrestrial ferrobasalts. As anticipated in Chevrel et al. (2012), the viscosity of martian basalts is between 0.5 and 1 order of magnitude lower than terrestrial tholeiitic basalts at all magmatic temperatures.

6. DISCUSSION

The viscosity of all studied compositions are less than 1 Pa s at liquidus temperatures. The magma rise speed may be calculated from equations given in Wilson et al. (2009). With such low values of viscosity, the Reynolds

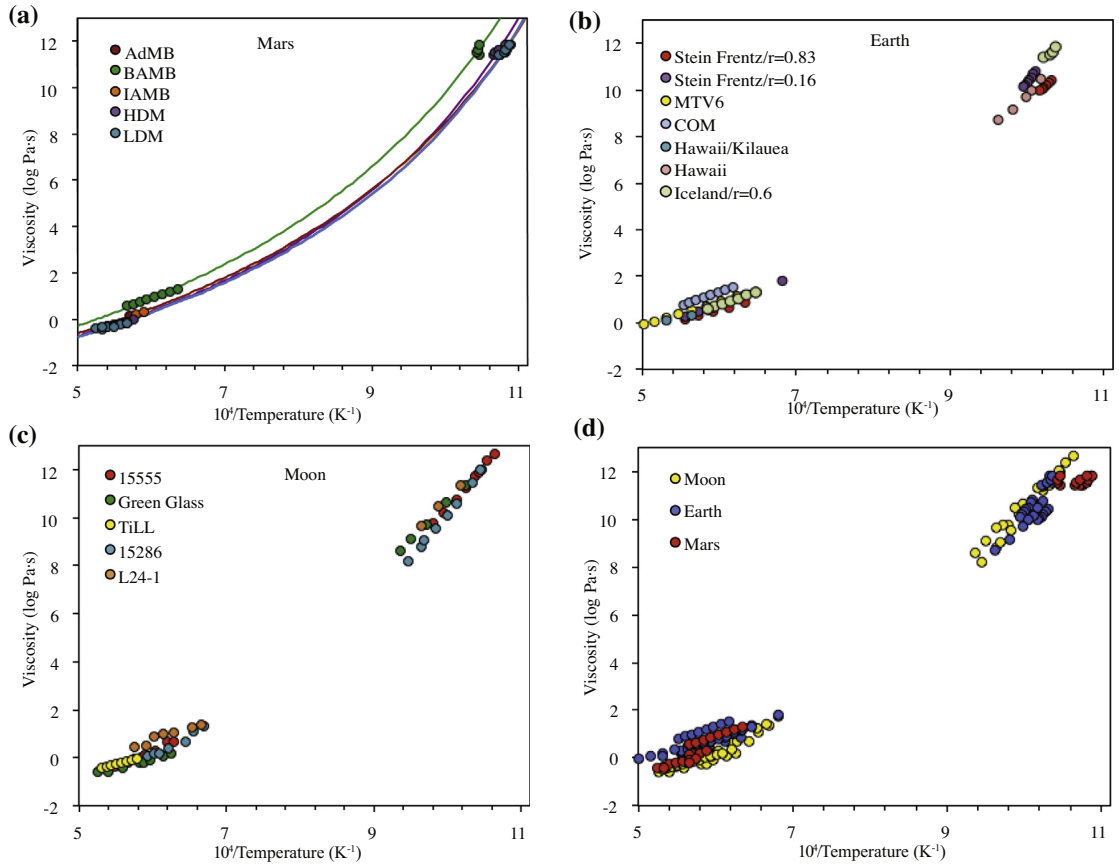

Fig. 9. Viscosity data for martian, lunar and terrestrial basaltic melts. (a) Viscosity data points under low fO_2 and fitting TVF curves for the investigated martian melts. (b) Terrestrial Fe-rich basaltic melts including natural basalts from Western Volcanic Zone Iceland and from Craters of The Moon, USA (Iceland and COM, respectively; personal unpublished data); from Hawaii (Hawaii/Kilauea is from Kushiro et al., 1976 and Hawaii is R839-5.8 from Gottsmann et al., 2002) and basalt from Stein Frentz with two different redox state (Bouhifd et al., 2004); a synthetic ferro-basalt (MTV; Toplis et al., 1994); $r = FeO/FeO_{tot}$. (c) Synthetic basalts from the Moon including the primitive basalt (15555) from Cukierman et al. (1973), the green glass from Apollo 15 (Uhlmann et al., 1974), the Ti-rich basalt from Apollo 11 (TiLL, Murase and McBirney, 1970), a basaltic glass (15286) from Uhlmann and Klein (1976); and a mare basalt (L-24) from Handwerker et al. (1978). (d) Comparison of all the compiled data.

number is above 2000 and the flow within the magma conduit is turbulent. Considering equations for turbulent flows, a dyke width of 3 m, and a pressure gradient of 500 Pa/m as in Wilson et al. (2009), the magma rise speed appears to be greater than 10 m/s (or even higher if shear heating takes place). These values are significantly faster than estimates of Wilson et al. (2009) who considered a viscosity of 100 Pa s. Cooling will be therefore negligible during magma ascent. Fractional crystallization should therefore remain limited as long as the magma remains buoyant. Crustal contamination and chemical interactions with the host rocks should be also limited for the same reasons. These low viscosities may be one of the key parameters to explain the abundance of primitive magmas at the surface of Mars (McSween et al., 2006b; Baratoux et al., 2011) and the abundance of olivine in comparison with our planet (Poulet et al., 2009).

Magmas are polyphase materials composed of a viscous melt and suspended particles (crystals and bubbles). Their apparent viscosity is therefore a combination of the melt viscosity and the effect of the particles (e.g., Shaw, 1969; Murase and McBirney, 1973; Ryerson et al., 1988; Petford, 2009). If the particle concentration is low (below the critical volume fraction depending on the crystals shape and size distribution) the physical behavior of the magma is controlled by the viscosity of the melt phase that is Newtonian (Lejeune and Richet, 1995; Costa et al., 2009). When the crystal fraction becomes too high, the viscosity is no longer controlled by the melt but by the particles network and become non-Newtonian, strain-rate dependent (Caricchi et al., 2007; Lavallée et al., 2007; Costa et al., 2009; Petford, 2009; Cordonnier et al., 2012). The viscosity of a flowing basaltic lava increases during emplacement and cooling, in a way that depends on the crystallization sequence (e.g., Shaw, 1969; Marsh, 1981; Pinkerton and Stevenson, 1992; Crisp et al., 1994; Villeneuve et al., 2008). A basaltic cooling-limited lava flow ceases flowing when its viscosity reach a critical value associated with the interlocking of the crystals network (near the random maximum packing of crystals; e.g., Shaw, 1969; Murase and McBirney, 1973; Marsh, 1981; Crisp et al., 1994). The following section offers a framework to interpret the diversity of volcanic

landforms on Mars and explore in which cases variations in lava flow morphology may be comfortably related to variations in chemistry.

For this purpose, the viscosity of the magma (melt + crystals) is calculated during the crystallization sequence for all the investigated compositions (except HDM that is similar to AdMB). The melt phase is calculated using the most appropriate model for martian compositions, namely the GRD model as demonstrated previously. The effect of crystals is determined using the most sophisticated approach taking into account two populations of crystals with various shapes and the non-Newtonian behavior of crystal bearing magmas (Costa et al., 2009, using the fit of Cimarelli et al., 2011). The first calculation, considers two populations of crystals: the mafic minerals approximated with spherical shape and the plagioclase approximated a needle-like shape. A second calculation estimates the viscosity increase attributed to crystallization of needle-like shape for mafic crystals corresponding to the formation of spinifex textures, that is likely to happen in magma with high-normative olivine content (Bertka and Holloway, 1994; Bost et al., 2012). In both cases, the strain rate is held constant at 1 s^{-1} that is reasonable value for natural basaltic lava flow (Crisp et al., 1994).

The crystallization sequence can be directly modeled using the low-pressure MELTS algorithm (Ghiorso and Sack, 1995). According to petrographic observations of the martian basalts and to experimental petrology, the surface conditions are estimated by Monders et al. (2007) and Herd et al. (2002) to be 1 bar under an oxygen fugacity of QFM-1. The validation of using MELTS for Gusev basalts, was tested by Monders et al. (2007) and shows good agreement with experimental trend, although they do not recommend the use of MELTS to calculate the liquid lines of descent after a certain amount of crystallization, when the residual liquid become too Fe-rich. Baratoux et al. (2013) showed that mineral assemblages crystallizing at these conditions from primary mantle melts correspond to the observed mineralogy at the Mars' surface consisting in general of olivine, plagioclase, and a two-pyroxene assemblage (Poulet et al., 2009). Moreover, the observed evolution of the ratio of the low-calcium pyroxene (LCP) to the high-calcium pyroxene (HCP) end-members from the Late Noachian to the Amazonian periods would appear as a consequence of the evolution of the conditions of melting (Baratoux et al., 2011) associated with planetary cooling (Baratoux et al., 2013). We observe in Fig. 10 that AdMB that has a similar crystallization sequence as HDM with the two-pyroxene assembly typical of old martian terrains. The crystallization of the LDM composition exhibits, as in the case of komatiites, a very large temperature difference between the liquidus and solidus temperature, that is over 300 °C. The crystallization sequence of the trachy-basalt is distinguishable from the others with the lower proportion of pyroxene (15%) and a large proportion of feldspar.

Fig. 11 shows the increase of viscosity for the four compositions as temperature decreases and crystallization takes place. A sharp increase of viscosity with temperature occurs when the crystal fraction approaches the maximum crystal packing. The rate of the increase of apparent viscosity with temperature starts decreasing at a critical crystal fraction defining the rheological transition where the viscous

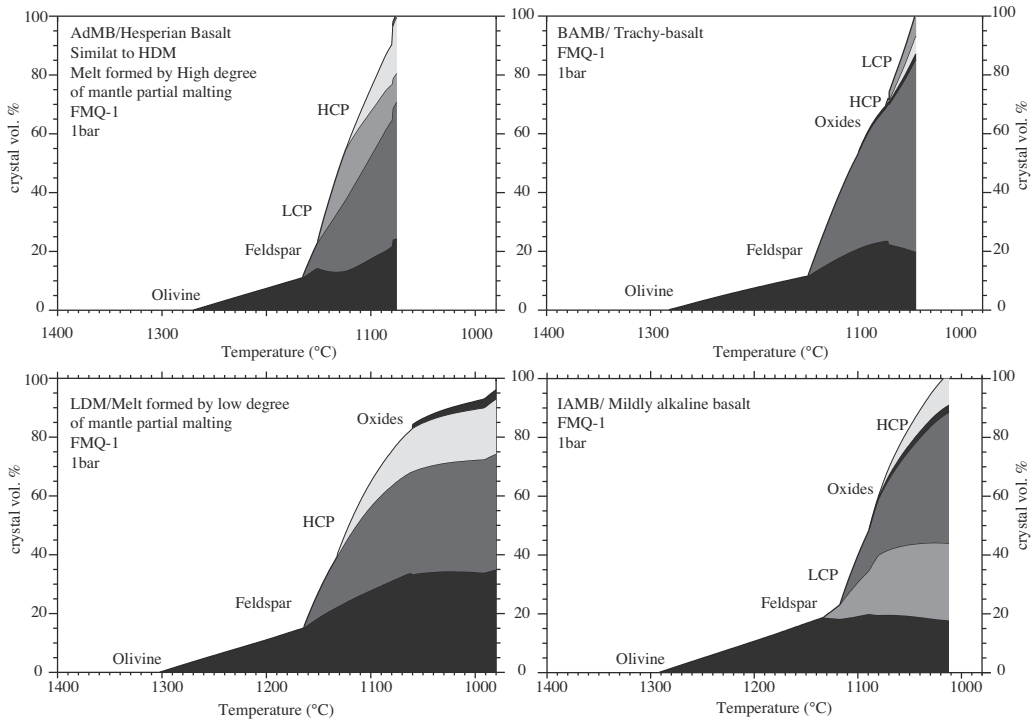

Fig. 10. Crystallization sequence at 1 bar and QFM-1 for all investigated compositions. The sample HDM is not shown, as its crystallization sequence is nearly identical to AdMB.

behavior is no longer controlled by the melt but by the solid framework (e.g., Lejeune and Richet, 1995; Costa et al., 2009). This transition is the rheological limit of flow advance, which is likely to be recorded in the final morphology of the lava flow (Giordano et al., 2007; Chevrel et al., 2013). We note that the range of viscosity obtained here is in agreement with typical viscosities of martian lava flows obtained from morphometric analyses (Hauber et al., 2011; Pasckert et al., 2012; Grott et al., 2013 and references herein).

Although the melt formed by low degree of partial melting (LDM) has a lower viscosity than the one formed by high degree of partial melting (HDM), the viscous behavior during crystallization and the rheological limits at the critical crystal fraction are very similar (10^5–$10^{5.2}$ Pa s; Fig. 11). This result indicates that it would be very difficult to distinguish these two types of lava from their flow morphology. However, the calculated viscosity at the maximum packing for these lavas in case needle-shape crystals would crystallize (in particular as formed in spinifex texture) would be around $10^{3.5}$ Pa s as a result for a lower critical maximum packing value. Differences in lava flow apparent viscosity could then also be attributed to variable rates of cooling and crystallization influencing the ability to produce spinifex texture rather than to differences between the viscosities of the liquid phase. In detail, a silicate melt able to crystallize spinifex-needle-like crystals would be interpreted as having a low apparent viscosity using equations for the emplacement of an isothermal Newtonian fluid (as the maximum crystals packing is reduced in the presence of needles). In this respect, the extremely low values of apparent viscosity obtained for some recent lava flows in the Central Elysium Planitia, on Mars (10^2 Pa s; Vaucher et al., 2009b) are at the extreme lower limits of our range of predictions.

A larger viscosity difference between the primitive basalts and the more alkaline-rich-basalt is found with expected values of 0.5 log unit at superliquidus regime and 1–3 log units at the crystal maximum packing (10^6–10^8 Pa s). A factor of two for the magma rise speed is expected from the slight differences at magmatic temperature between primitive basalts and the more alkaline-rich-basalts. The larger difference at maximum packing suggests that the morphology of alkaline-rich lavas may be distinguished from that of tholeiitic lava. A fraction or all of the upper range of lava flows for which inferred viscosities were found above 10^6 Pa s may be proposed as candidates for the expression of effusive and alkali-rich basalts, revealed by a minority of volcanic rocks at Gusev craters and by new observations at Gale crater made by the rover Curiosity (Sautter et al., submitted). Therefore, one does not need to invoke the occurrence of basaltic-andesite or andesite lavas to explain these relatively high viscosity values. Morphological, chemical, and mineralogical observations of volcanic provinces on Mars are therefore reconciled within this new rheological framework, as the diversity of lava flow morphologies would correspond to basaltic compositions with variable contents of alkaline elements. This conclusion is also compatible with the study of Warner and Gregg (2003) who estimated the viscosity of an andesitic lava flow from Sabancaya volcano (Peru) to be 10^{10}–10^{12} Pa s and therefore reject the possibility that lava flow on Mars having viscosity of 10^6 Pa s could be andesitic.

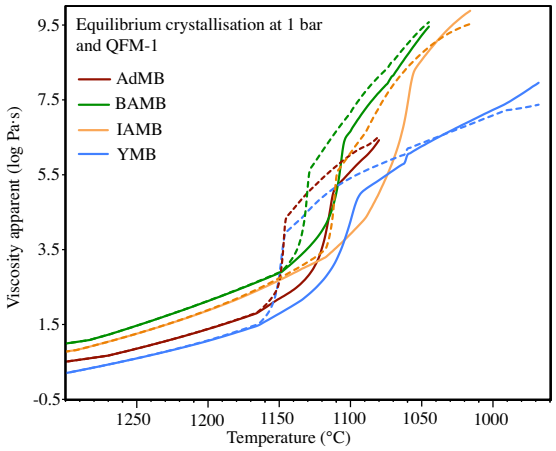

Fig. 11. Apparent viscosity of martian lavas as a function of temperature taking into account the crystallization sequence. The bold lines are calculation for two populations of crystals (mafic minerals being considered as spheres and feldspar as needles) and dashed line are calculation for all crystals being considered as needles (to mimic spinifex texture).

7. CONCLUSION

The viscosity measurements of iron-rich synthetic melts representing the diversity of basaltic rocks found on Mars' surface indicate viscosities similar to some Fe-rich basaltic terrestrial and lunar lavas. A comparison with rheological empirical models available in the literature reveals that the GRD model (Giordano et al., 2008) is the best to reproduce experimental data at both superliquidus regime and near the glass transition while Shaw (1972) model is only suitable for high temperature and the model of Hui and Zhang (2007) shows very large discrepancies. Estimation of the apparent viscosity of crystallizing lavas is in agreement with most of the value calculated from lava flow morphology on Mars surface. The difference in chemical composition of primary melts formed by various degrees of mantle partial melting does not lead to major viscosity variations and may not be recognized from their apparent viscosity calculated from the morphological dimensions. Low apparent viscosity (10^2–10^4 Pa s) inferred from the morphology would be rather attributed to komatiite-like lava flows and the higher values (10^6–10^8 Pa s) may be associated to alkaline-rich lavas rather than Si-rich compositions.

ACKNOWLEDGEMENTS

M.O. Chevrel wishes to thank THESIS (Elitenetzwerk Bayern) for financial support. D. Baratoux is supported by the Programme National de Planétologie. D.B. Dingwell was supported by a research professorship of the Bundesexzellenzinitiative (LMUexcellent) and an Advanced Grant of the European Research Council (EVOKES – 247076).

APPENDIX A. SUPPLEMENTARY DATA

Supplementary data associated with this article can be found, in the online version, at http://dx.doi.org/10.1016/j.gca.2013.08.026.

REFERENCES

Anderson D. L. (1972) Internal constitution of Mars. *J. Geophys. Res.* **77**, 789–795.

Angell C. (1985) *Strong and Fragile Liquids Relaxations in Complex Systems*. U.S. Department of Commerce National Technical Information Service, Springfield, VA, 3–11.

Arndt N., Naldrett A. and Pyke D. (1977) Komatiitic and iron-rich tholeiitic lavas of Munro Township, Northeast Ontario. *J. Petrol.* **18**(part 2), 319–369.

Baratoux D., Pinet P., Toplis M. J., Mangold N., Greeley R. and Baptista A. R. (2009) Shape, rheology and emplacement times of small Martian shield volcanoes. *J. Volcanol. Geotherm. Res.* **185**, 47–68.

Baratoux D., Toplis M. J., Monnereau M. and Gasnault O. (2011) Thermal history of Mars inferred from orbital geochemistry of volcanic provinces. *Nature* **472**, 338–341.

Baratoux D., Toplis M. J., Monnereau M. and Sautter V. (2013) The petrological expression of early Mars volcanism. *J. Geophys. Res.* **118**, 1–6.

Bertka C. and Holloway J. (1994) Anhydrous partial melting of an iron-rich mantle ii: primary melt compositions at 15 kbar. *Contrib. Mineral. Petrol.* **115**, 323–338.

Binder A. (1976) On the compositions and characteristics of the mare basalt and their source regions. *The Moon* **16**, 115–150.

Bost N., Westall F., Gaillard F., Ramboz C. and Foucher F. (2012) Synthesis of a spinifex-textured basalt as an analog to Gusev Crater basalts, Mars. *Meteorit. Planet. Sci.*, 1–12.

Bouhifd A., Richet P., Besson P., Roskosz M. and Ingrin J. (2004) Redox state, microstructure and viscosity of a partially crystallized basalt melt. *Earth Planet. Sci. Lett.* **218**, 31–44.

Boynton W. V., Taylor G. J., Evans L. G., Reedy R. C., Starr R., Janes D. M., Kerry K. E., Drake D. M., Kim K. J., Williams R. M. S., Crombie M. K., Dohm J. M., Baker V., Metzger A. E., Karunatillake S., Keller J. M., Newsom H. E., Arnold J. R., Brückner J., Englert P. A. J., Gasnault O., Sprague A. L., Mitrofanov I., Squyres S. W., Trombka J. I., d'Uston L., Wänke H. and Hamara D. K. (2007) Concentration of H, SI, CL, K, FE, and TH in the low- and mid-latitude regions of mars. *J. Geophys. Res.* **112**, E12S99.

Caricchi L., Burlini L., Ulmer P., Gerya T., Vassalli M. and Papale P. (2007) Non-Newtonian rheology of crystal-bearing magmas and implications for magma ascent dynamics. *Earth Planet. Sci. Lett.* **264**, 402–419.

Chevrel M. O., Giordano D., Potuzak M., Courtial P. and Dingwell D. B. (2012) Physical properties of $CaAl_2Si_2O_8$–$CaMgSi_2O_6$–FeO–Fe_2O_3 melts: analogues for extra-terrestrial basalt. *Chem. Geol.* **346**, 93–105.

Chevrel M. O., Platz T., Hauber E., Baratoux D., Lavallée Y. and Dingwell D. B. Planetary lava flow: a comparison of morphological and petrological methods. *Earth Planet. Sci. Lett.* (accepted), 2013.

Cimarelli C., Costa A., Mueller S. and Mader H. M. (2011) Rheology of magmas with bimodal crystal size and shape distributions: insights from analog experiments. *Geochem. Geophys. Geosyst.* **12**, Q07024.

Cordonnier B., Caricchi L., Pistone M., Castro J., Hess K. U., Gottschaller S., Manga M., Dingwell D. B. and Burlini L. (2012) The viscous-brittle transition of crystal-bearing silicic melt: direct observation of magma rupture and healing. *Geology* **40**, 611–614.

Costa A., Caricchi L. and Bagdassarov N. (2009) A model for the rheology of particle-bearing suspensions and partially molten rocks. *Geochem. Geophy. Geosyst.* 10, Q03010, doi: 10.1029/2008GC002138.

Crisp J., Cashman K. V., Bonini J. A., Hougen S. and Pieri D. (1994) Crystallization history of the 1984 Mauna Loa lava flow. *J. Geophys. Res.* **99**, 7177–7198.

Cukierman M., Klein L., Scherer G., Hopper R. W. and Uhlmann D. R. (1973) Viscous flow and crystallization behavior of selected lunar composition. *Geochim. Cosmochim. Acta* **3**, 2685–2696.

Cukierman M., Tutts P. M. and Uhlmann D. R. (1972) Viscous flow behavior of lunar composition 14259 and 14310. *Geochim. Cosmochim. Acta* **3**, 2619–2625.

Dingwell D. B. (1986) Viscosity–temperature relationships in the system $Na_2Si_2O_5$–$Na_4Al_2O_5$. *Geochim. Cosmochim. Acta* **50**, 1261–1265.

Dingwell D. B. (1996) Volcanic dilemma: flow or blow. *Science* **273**, 1054–1055.

Dingwell D. B. and Virgo D. (1987) The effect of oxidation state on the viscosity of melts in the system Na_2O–FeO–Fe_2O_3–SiO_2. *Geochim. Cosmochim. Acta* **51**, 195–205.

Dreibus G. and Wänke H. (1984) Accretion of the earth and the inner planets. *Geochem. Cosmochem.*, 1–20.

Dreibus G. and Wänke H. (1985) Mars, a volatile-rich planet. *Meteoritics* **20**, 367–381.

Eason D. E. and Sinton J. M. (2009) Lava shields and fissure eruptions of the Western Volcanic Zone, Iceland: evidence for magma chambers and crustal interaction. *J. Volcanol. Geotherm. Res.* **186**, 331–348.

El Maarry M., Gasnault O., Toplis M., Baratoux D., Dohm J., Newsom H., Boynton W. and Karunatillake S. (2009) Gamma-ray constraints on the chemical composition of the Martian surface in the Tharsis region: a signature of partial melting of the mantle?. *J. Volcanol. Geotherm. Res.* **189** 116–122.

Elkins-Tanton L. T., Hess P. C. and Parmentier E. M. (2005) Possible formation of ancient crust on Mars through magma ocean processes. *J. Geophys. Res. (Planets)* **110**, E12S01.

Eyring H., Henderson D., Stover B. and Eyring E. (1982) *Statistical mechanics and dynamics*, second ed. John Wiley, NY.

Fisk M. R., Bence A. and Schilling J.-G. (1982) Major element chemistry of Galapagos rift zone magmas and their phenocrysts. *Earth Planet. Sci. Lett.* **61**, 171–189.

Francis D., Ludden J., Johnstone R. and Davis W. (1999) Picrite evidence for more Fe in Archean mantle reservoirs. *Earth Planet. Sci. Lett.* **167**, 197–213.

McSween H., Taylor G. J. and Wyatt M. B. (2009) Elemental composition of the martian crust. *Science* **324**, 736.

Monders A. G., Médard E. and Groove T. L. (2007) Phase equilibrium investigations of the Adirondack class basalts from the Gusev plains, Gusev crater, Mars. *Meteorit. Planet. Sci.* **42**, 131–148.

Mysen B. O. (1991) Relation between structure, redox equlibria of iron, and properties of magmatic liquids. *Adv. Phys. Chem.* **9**, 41–98.

Gellert R., Rieder R., Anderson R. C., Brückner J., Clark B. C., Dreibus G., Economou T., Klingelhöfer G., Lugmair G., Ming D. W., Squyres S. W., d'Huston C., Wänke H., Yen A. and Zipfel J. (2004) Chemistry of rocks and soils in Gusev crater from the Alpha Particle X-ray Spectrometer. *Science* **305**, 829–832.

Gellert R., Rieder R., Brückner J., Clark, B. C., Dreibus G., Klingelhöfer G., Lugmair G., Ming D. W., Wänke H., Yen A., Zipfel J. and Squyres S. W. (2006) Alpha Particle X-ray

Spectrometer (APXS): results from Gusev crater and calibration report. *J. Geophys. Res.* **111**, E02S05, doi: 10.1029/2005JE002555.

Ghiorso M. S. and Sack O. (1995) Chemical mass transfer in magmatic processes IV. A revised and internally consistent thermodynamic model for the interpolation and extrapolation of liquid–solid equilibria in magmatic systems at elevated temperatures and pressures. *Contrib. Mineral. Petrol.* **119**, 197–212.

Gibson S., Thompson R. and Dickin A. (2000) Ferropicrites: geochemical evidence for Fe-rich streaks in upwelling mantle plumes. *Earth Planet. Sci. Lett.* **174**, 355–374.

Giordano D., Polacci M., Longo A., Papale P., Dingwell D. B., Boschi E. and Kasereka M. (2007) Thermo-rheological magma control on the impact of highly fluid lava flows at Mt. Nyiragongo. *Geophys. Res. Lett.* **34**, L06301.

Giordano D., Russell J. K. and Dingwell D. B. (2008) Viscosity of magmatic liquids: a model. *Earth Planet. Sci. Lett.* **271**, 123–134.

Giuli G., Paris E., Pratesi G., Hess K. U., Dingwell D., Cicconi M., Eeckhoult S., Fehr K. and Valenti P. (2011) XAS determination of the Fe local environment and oxidation state in phonolite glasses. *Am. Mineral.* **96**, 631636.

Gottsmann J., Giordano D. and Dingwell D. B. (2002) Predicting shear viscosity during volcanic processes at the glass transition: a calorimetric calibration. *Earth Planet. Sci. Lett.* **198**, 417–427.

Greeley R., Foing B. H., McSween H. Y., Neukum G., Pinet P., van Kan M., Werner S. C., Williams D. A. and Zegers T. E. (2005) Fluid lava flows in Gusev crater, Mars. *J. Geophys. Res.* **110**, E05008.

Grott M., Baratoux D., Hauber E., Sautter V., Mustard J., Gasnault O., Ruff S. W., Karato S. I., Debaille V., Knapmeyer M., Sohl F., VanHoolst T., Breuer D., Morschhauser A. and Toplis M. J. (2013) Long-term evolution of the Martian crust-mantle system. *Space Sci. Rev.* **174**, 49–111.

Handwerker C. A., Onorato P. I. K. and Uhlmann D. (1978) Viscous flow, crystal growth, and glass formation of highland and mare basalts from Luna 24. *Mare Crisium: The view from Luna 24* in Pergamon Press (NY), 483–493.

Hartmann W. K., Malin M., McEwen A., Carr M., Soderblom L., Thomas P., Danielson E., James P. and Veverka J. (1999) Evidence for recent volcanism on Mars from crater counts. *Nature* **397**, 586–589.

Hauber A., Bleacher J., Gwinner K., Williams D. and Greeley R. (2009) Topography and morphology of low shields and associated landforms of plains volcanism in the Tharsis region of Mars. *J. Volcanol. Geotherm. Res.* **185**, 69–95.

Hauber E., Broz P., Jagert F., Jodlowski P. and Platz T. (2011) Very recent and wide spread basaltic volcanism on Mars. *Geophys. Res. Lett.* **38**, L10201.

Herd C. D. K., Borg L., Jones J. H. and Papike J. J. (2002) Oxygen fugacity and geochemical variations in the Martian basalts: implications for Martian basalt petrogenesis and the oxidation state of the upper mantle of Mars. *Geochim. Cosmochim. Acta* **66**, 2025–2036.

Hess K. U. and Dingwell D. (1996) Viscosities of hydrous leucogranitic melts: a non-Arrhenian model. *Am. Mineral.* **81**, 1297–1300.

Hiesinger H., Head J. W. and Neukum G. (2007) Young lava flows on the eastern flank of Ascraeus Mons: rheological properties derived from High Resolution Stereo Camera (HRSC) images and Mars Orbiter Laser Altimeter (MOLA) data. *J. Geophys. Res.* **112**, E05011.

Hui H. and Zhang Y. (2007) Toward a general viscosity equation for natural anhydrous and hydrous silicate melts. *Geochim. Cosmochim. Acta* **71**, 403–416.

Hurowitz J. A., McLennan S. C., Lindsley D. H. and Schoonen M. A. (2005) Experimental epithermal alteration of synthetic Los Angeles meteorite: implication for the origin of Martian soils and identification of hydrothermal sites on Mars. *J. Geophys. Res.* **110**, E07002.

Hynek B. M., Phillips R. J. and Arvidson R. E. (2003) Explosive volcanism in the Tharsis region: global evidence in the Martian geologic record. *J. Geophys. Res.* **108**, E95111.

Jaeger W. L., Keszthelyi L. P., McEwen A. S., Dundas C. W. and Russell P. S. (2007) Athabasca Valles, Mars: a lava-draped channel system. *Science* **317**, 1709–1711.

Jaeger W. L., Keszthelyi L. P., Skinner, Jr., J. A., Milazzo M. P., McEwen A. S., Titus T. N., Rosiek M. R., Galuszka D. M., Howington-Kraus E. and Kirk R. L.the HiRISE Team (2010) Emplacement of the youngest flood lava on Mars: a short, turbulent story. *Icarus* **205**, 230–243.

Karamanov A. and Pelino M. (2001) Crystallization phenomena in iron-rich glasses. *J. Non-Cryst. Solids* **281**, 139–151.

Karamanov A., Di Gioacchino R., Pisciella P., Pelino M. and Hreglich A. (2002) Viscosity of iron rich glasses obtained from industrial wastes. *Glass Technol.* **43**(1), 34–38.

Khan A. and Connolly J. A. D. (2008) Constraining the composition and thermal state of mars from inversion of geophysical data. *J. Geophys. Res.* **113**, E07003.

Kremers S., Lavallée Y., Hanson J., Hess K. U., Chevrel M. O., Wassermann J. and Dingwell D. B. (2012) Shallow magma-mingling-driven strombolian eruptions at Mt. Yasur volcano, Vanuatu. *Geophys. Res. Lett.* **39**, L21304.

Kushiro I., Yoder, Jr., H. and Mysen B. (1976) Viscosities of basalt and andesite melts at high pressures. *J. Geophys. Res.* **81**, 6351–6356.

Lavallée Y., Hess K. U., Cordonnier B. and Dingwell D. B. (2007) Non-Newtonian rheological law for highly crystalline dome lavas. *Geology* **35**, 843–846.

Lejeune A. M. and Richet P. (1995) Rheology of crystal-bearing silicate melts: an experimental study at high viscosities. *J. Geophys. Res.* **100**(B3), 4215–4229.

Leverington D. W. (2011) A volcanic origin for the outflow channels of mars: key evidence and major implications. *Geomorphology* **132**, 5175.

Marsh B. (1981) On the crystallinity, probability of occurrence, and rheology of lava and magma. *Contrib. Mineral. Petrol.* **78**, 85–98.

McSween H. Y., Arvidson R. E., Bell, III, J. F. and Blaney D., et al. (2004). *Science* **305**, 842.

McSween H. Y., Ruff S. W., Morris R. V., Bell J. F., Herkenhoff K., Gellert R., Stockstill K. R., Tornabene L. L., Squyres S. W., Crisp J. A., Christensen P. R., McCoy T. J., Mittlefehldt D. W. and Schmidt M. (2006a) Alkaline volcanic rocks from the Columbia hills, Gusev crater, Mars. *J. Geophys. Res.* **111**, E09S91.

McSween H. Y., Wyatt M. B., Gellert R. and Bell J. F., et al. (2006b) Characterization and petrologic interpretation of olivine-rich basalts at Gusev crater, Mars. *J. Geophys. Res.* **111**, E02S10.

Michaut C. (2011) Dynamics of magmatic intrusions in the upper crust: theory and applications to laccoliths on earth and the moon. *J. Geophys. Res. (Planets)* **305**(116), B05.

Michaut C., Baratoux D. and Thorey C. (2013) Evidence for magmatic intrusions and significant deglaciation at mid-latitude in the Northern Plains of Mars. *J. Geophys. Res. (Planets), Icarus* **225**, doi: 10.1016/j.icarus.2013.04.015.

Ming D. W., Gellert R., Morris R. V., Arvidson R. E., Brückner J., Clark B. C., Cohen B. A., d'Uston C., Economou, T., Fleischer I., Klingelhöfer G., McCoy T. J., Mittlefehldt D. W., Schmidt M. E., Schröder C., Squyres, S. W., Tréguier E., Yen A. S. and

Zipfel J. (2008) Geochemical properties of rocks and soils in Gusev crater, Mars: results of the Alpha Particle X-ray Spectrometer from Cumberland Ridge to Home Plate. *J. Geophys. Res.* **113**, E12S39.

Moynihan C. (1995) Structural relaxation and the glass transition. In *Structure, Dynamics and Properties of Silicate Melts* (eds. J. F. Stebbins, P. F. McMillan and D. B. Dingwell). Reviews in Mineralogy, Mineralogical Society of America, Chantilly, Virginia, pp. 1–19.

Moynihan C. T., Easteal A. J., Wilder J. and Tucker J. (1974) Dependence of glass transition temperature on heating and cooling rate. *J. Phys. Chem.* **78**(26), 2673–2677.

Murase T. and McBirney A. (1970) Viscosity of lunar lavas. *Science* **167**(3924), 1491–1493.

Murase T. and McBirney A. (1973) Properties of some common igneous rocks and their melts at high temperatures. *Geol. Soc. Am. Bull.* **84**, 3563–3592.

Myuller R. (1955) A valence theory of viscosity and fluidity for high-melting glass forming materials in the critical temperature range. *Zh. Prikl. Khim.* **28**, 1077–1087.

Norman M. and Garcia M. (1999) Primitive magmas and source characteristics of the Hawaiian plume: petrology and geochemistry of shield picrites. *Earth Planet. Sci. Lett.* **168**, 2744.

Page D. (2008) Comments on Athabasca Valles, Mars: A lava-draped channel system. *Science* **320**, 1588b.

Page D. (2010) Resolving the Elysium controversy: an open invitation to explain the evidence. *Planet. Space Sci.* **58**, 1406–1413.

Pasckert J. H., Hiesinger H. and Reiss D. (2012) Rheologies and ages of lava flows on Elysium Mons, Mars. *Icarus* **219**, 443–457.

Petford N. (2009) Which effective viscosity? *Mineral. Mag.* **73**, 167–191.

Philpotts A. R. (1977) Silicate liquid immiscibility in tholeiitic basalts. *J. Petrol.* **20**(part 1), 99–118.

Philpotts A. R. (2008) Comments on: Liquid immiscibility and the evolution of basaltic magma. Silicate Liquid Immiscibility in Tholeiitic Basalts. *J. Petrol.* **49**, 2171–2175.

Pinkerton H. and Stevenson R. J. (1992) Methods of determining the rheological properties of magmas at sub-liquidus temperatures. *J. Volcanol. Geotherm. Res.* **53**, 47–66.

Poulet F., Mangold N., Platevoet B., Bardintzeff J. M., Sautter V., Mustard J., Bibring J., Pinet P., Langevin Y., Gondet B. and Aléon-Toppani A. (2009) Quantitative compositional analysis of Martian mac regions using the MEX/OMEGA reflectance data 2. Petrological implications. *Icarus* **201**, 84–101.

Rieder R., Gellert R., Anderson R. C., Brückner J., Clark B. C., Dreibus G., Economou T., Klingelhöfer G., Lugmair G. W., Ming D. W., Squyres S. W., d'Uston C., Wänke H., Yen A. and Zipfel J. (2004) Chemistry of rocks and soils at Meridiani Planum from the Alpha Particles X-Ray Spectrometer. *Science* **306**, 1746–1749.

Roedder E. (1978) Silicate liquid immiscibility in magmas and in the system K_2O–FeO–Al_2O_3–SiO_2: en example of serendipity. *Geochem. Cosmochim. Acta* **42**, 1597–1617.

Russell J. and Giordano D. (2005) A model for silicate melt viscosity in the system $CaMgSi_2O_6$–$CaAl_2Si_2O_8$–$NaAlSi_3O_8$. *Geochim. Cosmochim. Acta* **69**, 5333–5349.

Russell J., Giordano D. and Dingwell D. B. (2003) High-temperature limits on viscosity of non-Arrhenian silicate melts. *Am. Min.* **88**, 1390–1394.

Russell J., Giordano D., Dingwell D. B. and Hess K. U. (2002) Modeling the non-Arrhenian rheology of silicate melts: numerical considerations. *Eur. J. Mineral.* **14**, 417–427.

Ryerson F. J., Weed H. C. and Piwinskii A. J. (1988) Rheology of subliquidus magmas: I picritic compositions. *J. Geophys. Res.* **93**, 3421–3436.

Sautter et al., Igneous mineralogy at Bradbury rise: the first ChemCam campaign, submitted to JGR-Planets.

Scherer G. (1984) Use of the Adam–Gibbs equation in the analysis of structural relaxation. *J. Am. Ceram. Soc.* **67**, 504–511.

Shaw H. R. (1969) Rheology of basalt in the melting range. *J. Petrol.* **10**, 510–535.

Shaw H. R. (1972) Viscosities of magmatic silicate liquids: an empirical method of prediction. *Am. J. Sci.* **272**, 870–893.

Stout M. Z., Nicholls J. and Kuntz M. A. (1994) Petrological and mineralogical variations in 2500–2000 yr B.P. Lava Flows, Crater of the Moon, Idaho. *J. Petrol.* **35**(Part 6), 1681–1715.

Taisne B., Tait S. and Jaupart C. (2011) Conditions for the arrest of a vertical propagating dyke. *Bull. Volcanol.* **73**, 191–204.

Tosca N. J., McLennan S. M., Lindsley D. H. and Schoonen M. A. A. (2004) Acid-sulfate weathering of synthetic Martian basalt: the acid fog model revisited. *J. Geophys. Res.* **109**, E05003.

Uhlmann D. R. and Klein L. (1976) Crystallization kinetics, viscous flow, and thermal histories of lunar breccias 15286 and 15498. *Proc. Lunar Sci. Conf, 7th*, 2529–2541.

Uhlmann D. R., Klein L., Kritchevsky G. and Hopper R. W. (1974) The formation of lunar glasses. *Geochim. Cosmochim. Acta* **Suppl. 3**, 2317–2331.

Vaucher J., Baratoux D., Mangold N., Pinet P., Kurita K. and Grégoire M. (2009a) The volcanic history of central Elysium Planitia: implications for martian magmatism. *Icarus* **204**, 418–442.

Vaucher J., Baratoux D., Toplis M. J., Pinet P., Mangold N. and Kurita K. (2009b) The morphologies of volcanic landforms at central Elysium Planitia: evidence for recent and fluid lavas on Mars. *Icarus* **200**, 39–51.

Veksler I. V. (2009) Extreme iron enrichment and liquid immiscibility in mafic intrusions: experimental evidence revisited. *Lithos* **111**, 72–82.

Veksler I. V., Dorfman A. M., Borisov A. A., Wirth R. and Dingwell D. B. (2007) Liquid immiscibility and the evolution of basaltic magma. *J. Petrol.* **48**, 2187–2210.

Veksler I. V., Dorfman A. M., Borisov A. A., Wirth R. and Dingwell D. B. (2008) Liquid immiscibility and evolution of basaltic magma: Reply to S. A. Morse, A. R. Mcbirney and A R.. *J. Petrol.* **49**, 2177–2186.

Villeneuve N., Neuville D. R., Boivin P., Bachèlery P. and Richet P. (2008) Magma crystallization and viscosity: a study of molten basalts from the Piton de la Fournaise volcano (La Réunion island). *Chem. Geol.* **256**, 242–251.

Warner N. H. and Gregg T. K. P. (2003) Evolved lavas on Mars? Observations from southwest Arsia Mons and Sabancaya volcano. *Peru. J Geophys. res.* **108**(E10), 5112.

Wilson L., Mouginis-Mark P., Tyson S., Mackown J. and Garbeil H. (2009) Fissure eruptions in Tharsis, mars implications for eruption conditions and magma sources. *J. Volcanol. Geotherm. Res.* **185**, 28–46.

Wilson S., Koenig A. and Lowers H. (2012) A new basaltic glass microanalytical reference material for multiple techniques. *Microsc. Today* **20**, 12–16.

Yoder C. F. (2003) Fluid core size of mars from detection of the solar tide. *Science* **300**, 299–303.

Zipfel J., Anderson R., Brückner J., Clark B. C., Dreibus G., Economou T., Gellert R., Klingelhöfer G., Lugmair G., Ming D., Reider R., Squyres S. W., d'Uston C., Wänke H. and Yen A. (2004) APXS analyses of Bounce rock the first shergottites on Mars. *Meteorit. Planet. Sci.* **39**(Suppl.), A118.

Associate editor: Christian Koeberl